

Adaptive discretization of the stationary and incompressible Navier-Stokes equations by stabilized Finite Element Methods

Original

Adaptive discretization of the stationary and incompressible Navier-Stokes equations by stabilized Finite Element Methods / Berrone, Stefano. - In: COMPUTER METHODS IN APPLIED MECHANICS AND ENGINEERING. - ISSN 0045-7825. - 190:(2001), pp. 4435-4455.

Availability:

This version is available at: 11583/1397684 since:

Publisher:

Published

DOI:

Terms of use:

This article is made available under terms and conditions as specified in the corresponding bibliographic description in the repository

Publisher copyright

(Article begins on next page)

Adaptive discretization of stationary and incompressible Navier–Stokes equations by stabilized Finite Element Methods

Stefano Berrone

*Dipartimento di Ingegneria Aeronautica e Spaziale, Politecnico di Torino,
Corso Duca degli Abruzzi 24, 10129, Torino, Italy,
e-mail: sberrone@calvino.polito.it
home page: <http://calvino.polito.it/~sberrone>*

Abstract

We have derived a residual-based *a posteriori* error estimator for a stabilized finite element discretization of the stationary incompressible Navier Stokes equations with general boundary conditions. An adaptive algorithm based on this error estimator is discussed and tested on some analytical and physical problems. When possible we study precisely the behaviour of the effectivity index.

Key words: A posteriori error estimators, adaptive mesh-refinement techniques, Navier Stokes equations, bounds on the effectivity index.

1991 MSC: 65N30, 65N15, 65N50, 76D05, 76M10.

1 Introduction

In the numerical simulation of real flows many questions are still open. One of them is how to control the accuracy of a numerical approximation for the solution of equations modeling these phenomena and how to use the available computational facilities to reach the needed accuracy with the lowest possible computational and man time as well as memory requests. Very often engineers and physicists need to solve problems in computational fluid dynamics in which the overall accuracy is deteriorated by the presence of interior or boundary layers, shock fronts and complex geometries with corners. So, difficulties in a very little part of the computational domain may cause a considerable reduction of the overall accuracy of the solution. A natural remedy is to increase the number of grid-points in these critical regions and simultaneously place very few points where the solution is smooth, in order to balance accuracy

and efficiency. To reach this target, we need an easily computable *a posteriori* error estimator that gives us information on how to distribute the points in an efficient manner.

One of the most important goals in the analysis of an *a posteriori* error estimator is to establish an equivalence relation between it and the true error of the numerical solution, measured in a suitable norm. From the pioneering work of Babuška and Rheinboldt [3] many interesting results have been achieved (see, for instance, [1,9,19,21,26] and the references therein), but many aspects of this problem are still unclear. In the present work we focus our attention on some of them, in the frame of the residual-based error estimators for the stationary incompressible Navier-Stokes equations. Following Verfürth's work, we have derived in [4] an error estimator for a stabilized discretization [10] of the linear problem. Here, we carefully analyse the influence of the Reynolds number in the relation which expresses the equivalence between the error estimator and the true error. We perform this analysis by numerical experiments on a problem with an analytic solution. Next we present an adaptive algorithm based on this error estimator and discuss several aspects about its behaviour and, in particular, its effectivity index.

At last, in Section 7 we apply our algorithm to a classical CFD problem. Although in [4] we derived the error estimator and we studied its effectivity index for a linear model, when we apply these results to the non-linear Navier-Stokes equations we get good results matching with previous analysis.

2 Linear incompressible Navier-Stokes model

2.1 The continuous problem

With the aim of introducing the error estimator and describing its use, we prefer to avoid the difficulties of the non-linearity of the true Navier-Stokes equations and we proceed considering a linear, steady-state, incompressible model:

$$-\frac{1}{Re}\Delta \bar{u} + (\bar{a} \cdot \nabla) \bar{u} + \nabla \bar{p} = \bar{f} \quad \text{in } \Omega, \quad (1)$$

$$\nabla \cdot \bar{u} = 0 \quad \text{in } \Omega, \quad (2)$$

$$\bar{u} = 0 \quad \text{on } \Gamma_D, \quad (3)$$

$$\frac{1}{Re} \frac{\partial \bar{u}}{\partial \hat{n}} - p \hat{n} = \bar{g}_N \quad \text{on } \Gamma_N, \quad (4)$$

where: Re is the Reynolds number; Ω is a bounded domain in \mathbb{R}^2 with a regular boundary $\partial\Omega$ that belongs to the class $\mathcal{C}^{0,1}$ ($\partial\Omega$ can be locally described by Lipschitz continuous functions [13,18]); the boundary $\partial\Omega$ is split into two subsets Γ_D and Γ_N , where Γ_D is closed and the following conditions holds true: $\partial\Omega = \Gamma_D \cup \Gamma_N$, $\Gamma_D \cap \Gamma_N = \emptyset$ and $|\Gamma_D| \neq 0$; $\bar{a} \in [H^1(\Omega)]^2 \cap [L^\infty(\Omega)]^2$, $\bar{\nabla} \cdot \bar{a} = 0$ in $\bar{\Omega}$; $\hat{n} \cdot \bar{a} \geq 0$ on Γ_N , where \hat{n} is the usual unit outward normal vector to $\partial\Omega$; $\bar{f} \in [L^2(\Omega)]^2$; $\bar{g}_N \in [H^{\frac{1}{2}}(\Gamma_N)]^2$.

Let us first derive a weak formulation of problem (1-4). The functional spaces we deal with are the usual Sobolev space $H_{0,D}^1(\Omega) \stackrel{def}{=} \{v \in H^1(\Omega) : v|_{\Gamma_D} = 0\}$ and Lebesgue space $L_0^2(\Omega) \stackrel{def}{=} \{q \in L^2(\Omega) : \int_{\Omega} q \, d\Omega = 0\}$. Moreover we set $V \stackrel{def}{=} [H_{0,D}^1(\Omega)]^2$ and $Q \stackrel{def}{=} L_0^2(\Omega)$ if $|\Gamma_N| = 0$ or $Q \stackrel{def}{=} L^2(\Omega)$ if $|\Gamma_N| > 0$. If $|\Gamma_N| = 0$, the pressure p in (1) can be determined only up to an additive constant that we fix by seeking a pressure with a zero mean value. A weak formulation of the problem can be written as: *Find $[\bar{u}, p] \in V \times Q$ such that $\forall [\bar{v}, q] \in V \times Q$ one has :*

$$\frac{1}{Re} (\bar{\nabla} \bar{u}, \bar{\nabla} \bar{v}) + ((\bar{a} \cdot \bar{\nabla}) \bar{u}, \bar{v}) - (p, \bar{\nabla} \cdot \bar{v}) = (\bar{f}, \bar{v}) + (\bar{g}_N, \bar{v})_{\Gamma_N}, \quad (5)$$

$$(q, \bar{\nabla} \cdot \bar{u}) = 0, \quad (6)$$

where $(., .)$ denotes the usual inner product in $L^2(\Omega)$ or in $[L^2(\Omega)]^2$ and $(., .)_{\Gamma_N}$ denotes the inner product in $[L^2(\Gamma_N)]^2$. Existence and uniqueness of the solution for all positive Re follows from the usual *coercivity* inequality and *inf-sup* condition (see, e.g., [13]).

2.2 The discrete problem

In order to discretize problem (1-4), we assume Ω to be a polygonal domain and we introduce a regular family of partitions $\{\mathcal{T}_h\}_h$ of $\bar{\Omega}$ into triangles which satisfy the usual conformity and minimal-angle conditions [8]. It is useful to introduce the diameter h_T of the element $T \in \mathcal{T}_h$. The parameter h of the family $\{\mathcal{T}_h\}_h$ represents $h = \max_{T \in \mathcal{T}_h} h_T$. Let $V_h \subset V$ and $Q_h \subset Q$ be two conforming finite element spaces based on the partition \mathcal{T}_h . If we consider the pure Galerkin approximation of the continuous problem (5,6), we have to satisfy the discrete version of the *inf-sup* condition [6,13,18].

In what follows, we are going to use continuous finite elements for the velocity: $V_h \stackrel{def}{=} \left\{ \bar{v}_h \in V \cap [\mathcal{C}^0(\bar{\Omega})]^2 : \bar{v}_h|_T \in [P_k(T)]^2, \forall T \in \mathcal{T}_h \right\}$ and the pressure: $Q_h \stackrel{def}{=} \left\{ q_h \in Q \cap \mathcal{C}^0(\bar{\Omega}) : q_h|_T \in P_l(T), \forall T \in \mathcal{T}_h \right\}$. Here $P_i(T)$ is the space of polynomials of degree $i \geq 1$ on the element $T \in \mathcal{T}_h$. In the discretization of

the problem, we also consider approximations of the data \bar{a} , \bar{f} , \bar{g}_N by some interpolations $\Pi_T \bar{a}$, $\Pi_T \bar{f}$, $\Pi_E \bar{g}_N$ whose definition will be given later on. With an arbitrary choice of k and l these spaces may not satisfy the discrete *inf-sup* condition [6]. However, this difficulty may be avoided by resorting to a consistent modified approximation of the problem known as the *Streamline Upwind/Petrov Galerkin (SUPG)* method [10,11,15]: *Find $[\bar{u}_h, p_h] \in V_h \times Q_h$ such that $\forall [\bar{v}_h, q_h] \in V_h \times Q_h$ let be :*

$$\begin{aligned}
& \frac{1}{Re} \left(\nabla \bar{u}_h, \nabla \bar{v}_h \right) + \left(\left(\Pi_T \bar{a} \cdot \nabla \right) \bar{u}_h, \bar{v}_h \right) - \left(p_h, \nabla \cdot \bar{v}_h \right) \\
& + \sum_{T \in \mathcal{T}_h} \tau_T \left(-\frac{1}{Re} \Delta \bar{u}_h + \left(\Pi_T \bar{a} \cdot \nabla \right) \bar{u}_h + \nabla \bar{p}_h, \left(\Pi_T \bar{a} \cdot \nabla \right) \bar{v}_h \right)_T \\
& \quad + \sum_{T \in \mathcal{T}_h} \delta_T \left(\nabla \cdot \bar{u}_h, \nabla \cdot \bar{v}_h \right)_T \\
& = \left(\Pi_T \bar{f}, \bar{v}_h \right) + \left(\Pi_E \bar{g}_N, \bar{v}_h \right)_{\Gamma_N} + \sum_{T \in \mathcal{T}_h} \tau_T \left(\Pi_T \bar{f}, \left(\Pi_T \bar{a} \cdot \nabla \right) \bar{v}_h \right)_T, \quad (7) \\
& \left(q_h, \nabla \cdot \bar{u}_h \right) + \sum_{T \in \mathcal{T}_h} \tau_T \left(-\frac{1}{Re} \Delta \bar{u}_h + \left(\Pi_T \bar{a} \cdot \nabla \right) \bar{u}_h + \nabla \bar{p}_h, \nabla \bar{q}_h \right)_T \\
& \quad = \sum_{T \in \mathcal{T}_h} \tau_T \left(\Pi_T \bar{f}, \nabla \bar{q}_h \right)_T. \quad (8)
\end{aligned}$$

Here τ_T and δ_T depend on the local conditions of the flow in each element expressed by $Re_T \stackrel{def}{=} m_k \frac{\|\Pi_T \bar{a}\|_{\infty, T} h_T}{4 \frac{1}{Re}}$ and $m_k \stackrel{def}{=} \min \left\{ \frac{1}{3}, \frac{2}{C_*} \right\}$, C_* being the constant of the inverse inequality [14]: $h_T^2 \|\Delta v_h\|_{0, T}^2 \leq C_* \|\nabla v_h\|_{0, T}^2$, $\forall v_h \in V_h$. For linear elements, obviously, $m_k = \frac{1}{3}$. Practically, following [10] we set $\tau_T \stackrel{def}{=} m_k \frac{h_T^2}{8} Re$, $\delta_T \stackrel{def}{=} \lambda m_k \frac{\|\Pi_T \bar{a}\|_{\infty, T} h_T^2 Re}{4}$ if $0 \leq Re_T < 1$ and $\tau_T \stackrel{def}{=} \frac{h_T}{2 \|\Pi_T \bar{a}\|_{\infty, T}}$, $\delta_T \stackrel{def}{=} \lambda \|\Pi_T \bar{a}\|_{\infty, T} h_T$ if $Re_T \geq 1$. We take λ to be either 1 or 0, depending whether we want or we do not want to consider the terms multiplied by the parameter δ_T . By using the *SUPG* method, not only we circumvent the *inf-sup* condition [5,6,15], but also we stabilize the advective operator preventing the oscillations in the velocity field that appear for high Reynolds numbers [7,10,11].

3 A residual-based error estimator

In [4] we have derived a residual-based error estimator for our model problem following Verfürth's works [23,24,26,27,28]. Particularly, we have derived a global upper bound and a local lower bound for the error measured in an energy-like norm. Here, for space reasons, we only recall those results, but we invite the interested reader to look at [4] for a detailed description of the

hypotheses and methods used in the proofs. Let us recall some useful notations and definitions. For each edge E of the triangulation we consider a unit vector \hat{n}_E such that \hat{n}_E is orthogonal to E and equals the unit outward vector normal to $\partial\Omega$ if $E \subset \partial\Omega$. For any triangle $T \in \mathcal{T}_h$ let be $\mathcal{E}(T)$ the set of its edges,

$$\omega_T \stackrel{def}{=} \bigcup_{\{T': \mathcal{E}(T) \cap \mathcal{E}(T') \neq \emptyset\}} T' \quad \text{and} \quad \omega_E \stackrel{def}{=} \bigcup_{\{T': E \in \mathcal{E}(T')\}} T'.$$

Given any internal edge E and any $\varphi \in L^2(\omega_E)$ with $\varphi|_{T'} \in \mathcal{C}^0(\overline{T'}) \forall T' \in \omega_E$, we denote by $[\varphi]_E$ the jump of φ across E along the orientation of \hat{n}_E . Moreover:

$$\begin{aligned} \overline{\mathcal{T}} &\stackrel{def}{=} \overline{u}_h - \overline{u} \quad \text{and} \quad \overline{\Psi} \stackrel{def}{=} p_h - p, \\ \overline{R}_T([\overline{u}_h, p_h]) &\stackrel{def}{=} -\frac{1}{Re} \triangle \overline{u}_h + (\Pi_T \overline{a} \cdot \overline{\nabla}) \overline{u}_h + \overline{\nabla} p_h - \Pi_T \overline{f}, \\ \overline{R}_E([\overline{u}_h, p_h]) &\stackrel{def}{=} \left[\hat{n}_E \cdot \left(\frac{1}{Re} \overline{\nabla} \overline{u}_h - p_h \overline{\mathbf{I}} \right) \right]_E, \\ \overline{R}_{E,N}([\overline{u}_h, p_h], \Pi_E \overline{g}_N) &\stackrel{def}{=} \hat{n} \cdot \left(\frac{1}{Re} \overline{\nabla} \overline{u}_h - p_h \overline{\mathbf{I}} \right) - \Pi_E \overline{g}_N, \end{aligned}$$

At last, we give the definition of our residual-based *a posteriori* error estimator on the triangle $T \in \mathcal{T}_h$:

$$\begin{aligned} \eta_{R,T}^2 &\stackrel{def}{=} h_T^2 \left\| \overline{R}_T([\overline{u}_h, p_h]) \right\|_{0,T}^2 + \frac{1}{2} \sum_{E \in \mathcal{E}(T)} h_E \left\| \overline{R}_E([\overline{u}_h, p_h]) \right\|_{0,E}^2 + \\ &+ \sum_{E \in \mathcal{E}(T) \cap \mathcal{E}_{h,N}} h_E \left\| \overline{R}_{E,N}([\overline{u}_h, p_h], \Pi_E \overline{g}_N) \right\|_{0,E}^2 + \left\| \overline{\nabla} \cdot \overline{u}_h \right\|_{0,T}^2. \end{aligned} \quad (9)$$

We report the upper and lower bounds derived for the case $Re \gg 1$ and assuming that the problem is well a-dimensionalized, in the sense that $|\Omega| \preceq 1$, $\|\Pi_T \overline{a}\|_{\infty, \omega_T} \preceq 1$ and $\|\overline{a}\|_{\infty, \omega_T} \preceq 1$ for all $T \in \mathcal{T}_h$.

Proposition 1 *There exist two constants C^\uparrow and C_\downarrow , independent of any mesh-size and Reynolds number, but depending on the smallest angle of the triangulation, such that the global upper bound*

$$\begin{aligned} \left| \overline{\mathcal{T}} \right|_1 + \|\overline{\Psi}\|_0 &\leq C^\uparrow Re \left\{ \sqrt{\sum_{T \in \mathcal{T}_h} \eta_{R,T}^2} + \right. \\ &+ \left. \|\Pi_T \overline{a} - \overline{a}\|_\infty \|\overline{u}_h\|_1 + \left\| \Pi_T \overline{f} - \overline{f} \right\|_0 + \|\Pi_E \overline{g}_N - \overline{g}_N\|_{0, \Gamma_N} \right\} \end{aligned} \quad (10)$$

and the local lower bound

$$\eta_{R,T} \leq C_{\downarrow} \left\{ \left| \overline{\mathcal{T}} \right|_{1,\omega_T} + \|\Psi\|_{0,\omega_T} + h_T \left(\|\Pi_T \overline{a} - \overline{a}\|_{\infty,\omega_T} \|\overline{u}_h\|_{1,\omega_T} + \|\Pi_T \overline{f} - \overline{f}\|_{0,\omega_T} \right) + \sum_{E \in \mathcal{E}(T) \cap \mathcal{E}_{h,N}} \sqrt{h_E} \|\Pi_E \overline{g}_N - \overline{g}_N\|_{0,E} \right\} \quad (11)$$

hold true.

Remark 2 We notice that the constants C^{\uparrow} and C_{\downarrow} depend only on the constants in Cauchy-Schwarz's, Poincaré-Friedrichs', Young's and trace inequalities, as well as the constants of interpolation in Sobolev spaces and the inf – sup constant. All these constants are $\mathcal{O}(1)$, so we deduce that C^{\uparrow} and C_{\downarrow} are also $\mathcal{O}(1)$.

Remark 3 Inequalities (10,11) agree with results presented in [25,26] for the non-linear Navier-Stokes equations. Inequality (10) shows explicitly the dependence upon the Reynolds number of the constant appearing in the analogous estimates of [25,26]. Moreover in [4] we have considered the analogous estimates for the Stokes problem obtaining the same results of [23].

Remark 4 Comparing inequalities (10,11) with analogous estimates given in [23,24,25] or [2], we observe that the part of our approximation error concerning \overline{f} and \overline{g}_N is multiplied by a power of h that is different from those in the cited papers. This is due to the fact that we introduce the approximation of the data in the discretization of the problem as well, not only in the computation of the error estimator like in those works.

Remark 5 The results of Proposition 1 look to be non-optimal, since the the upper and lower bounds differ by the factor Re . In [28] the presence of the zero-order term in a scalar reaction-convection-diffusion equation allows the use of a more suitable energy-like norm for measuring the error, namely $\frac{1}{\sqrt{Re}} \|u_h - u\|_{\Omega,1} + \|u_h - u\|_{\Omega,0}$. The resulting upper and lower bounds differ only by the factor $c + \sqrt{Re} \|\overline{a}\|_{\infty,\Omega} \min\{h\sqrt{Re}, 1\}$, which is of the order of the local Re_T or \sqrt{Re} depending upon the flow conditions. Unfortunately, for the steady Navier-Stokes equations here considered, one cannot take advantage of any zero order term in the equations.

4 Equivalence between the true error and the error estimator

Looking forward to the use of the error estimator in the construction of a sequence of adapted Delaunay triangulations, we need some more considerations. At first we deal with some interpolations $\Pi_T \overline{f}$, $\Pi_T \overline{a}$ and $\Pi_E \overline{g}_N$ of the data \overline{f} , \overline{a} and \overline{g}_N with polynomials of degree n_1 , n_2 , $n_3 \geq 1$ respectively. Let

us suppose that for any triangulation \mathcal{T}_h under consideration and for suitable integers n_1, n_2, n_3 the following hypotheses hold:

$$\begin{aligned} \forall T \in \mathcal{T}_h, \quad & \bar{f}|_{\omega_T} \in [H^{n_1+1}(\omega_T)]^2, \\ \forall T \in \mathcal{T}_h, \quad & \bar{a}|_{\omega_T} \in [W^{n_2+1,\infty}(\omega_T)]^2, \\ \forall T \in \mathcal{T}_h : \exists E \subset \partial T \cap \Gamma_N \neq \emptyset, & \bar{g}_N|_E \in [H^{n_3+1}(T)]^2, \end{aligned}$$

where

$$W^{n+1,\infty}(\omega_T) \stackrel{def}{=} \{v \in L^\infty(\omega_T) : \partial^\alpha v \in L^\infty(\omega_T), \forall \alpha \in \mathbb{R}^2 : |\alpha| \leq n+1\};$$

moreover, we assume that the chosen interpolations satisfy following estimates:

$$\|\Pi_T \bar{f} - \bar{f}\|_{0,\omega_T} \lesssim h_T^{n_1+1} |\bar{f}|_{n_1+1,\omega_T}, \quad (12)$$

$$\|\Pi_T \bar{a} - \bar{a}\|_{0,\infty,\omega_T} \lesssim h_T^{n_2+1} |\bar{a}|_{n_2+1,\infty,\omega_T}, \quad (13)$$

$$\|\Pi_E \bar{g}_N - \bar{g}_N\|_{0,E} \lesssim h_E^{n_3+1} |\bar{g}_N|_{n_3+1,E}. \quad (14)$$

Furthermore we suppose that, using finite elements of the same order k for the velocity and the pressure, the true error

$$t.e. \stackrel{def}{=} |\bar{T}|_1 + \|\Psi\|_0 \quad (15)$$

decays, at most, proportionally to $h^{k+\frac{1}{2}}$. This agrees with the convergence results of the used stabilized method [10,18,22] (in the last two references we can see that a mesh-dependent norm of the true error for equal order finite elements behaves like h^k when $0 \leq Re_T \leq 1$ and like $h^{k+\frac{1}{2}}$ when $Re_T > 1$). At last, using (10) and (12-14) we conclude that it is possible to choose the degrees n_1, n_2, n_3 of interpolation for the data in such a way that, for any mesh-size h less than a certain \tilde{h} , the errors due to the approximation of the data appearing in inequalities (10,11) are negligible with respect to the global error estimator [2,17]

$$\eta_\Omega \stackrel{def}{=} \sqrt{\sum_{T \in \mathcal{T}_h} \eta_{R,T}^2}. \quad (16)$$

After these additional remarks we can use inequalities (10) and (11) to state the equivalence between the true error and the global error estimator, i.e.,

$$\underline{c} \eta_\Omega \leq |\bar{T}|_1 + \|\Psi\|_0 \leq \overline{C} Re \eta_\Omega, \quad (17)$$

where \underline{c} and \overline{C} depend upon C^\uparrow and C_\downarrow .

5 Sensitiveness to the Reynolds number

The theoretical analysis developed in [4] whose results are briefly recalled above, suggests an equivalence relation between our error estimator and the true error of the form

$$\underline{\mathcal{C}} \eta_\Omega \leq \left| \overline{\mathcal{T}} \right|_1 + \|\Psi\|_0 \leq \overline{\mathcal{C}} \eta_\Omega, \quad (18)$$

where $\underline{\mathcal{C}}$ and $\overline{\mathcal{C}}$ are two constants with respect to any mesh-size, but they may depend on the Reynolds number. Estimates (17) tell us that $\underline{\mathcal{C}}$ is bounded from below independently of Re , whereas $\overline{\mathcal{C}}$ is bounded from above by a linear function of Re . We now perform a numerical investigation of the behaviour of these constants. To this end, the effectivity index plays a fundamental role in the study of the equivalence relation between the error estimator and the true error; indeed, it is defined as the ratio between our global error estimator and the true error [2]:

$$e.i. \stackrel{def}{=} \frac{\eta_\Omega}{\left| \overline{\mathcal{T}} \right|_1 + \|\Psi\|_0}. \quad (19)$$

From inequalities (18) it follows that

$$\underline{\mathcal{C}} \leq \frac{1}{e.i.} = \frac{\left| \overline{\mathcal{T}} \right|_1 + \|\Psi\|_0}{\eta_\Omega} \leq \overline{\mathcal{C}}. \quad (20)$$

In the sequel we will perform a numerical study of the behaviour of the effectivity index and its inverse to get some indications on the values of $\underline{\mathcal{C}}$ and $\overline{\mathcal{C}}$. Taking into account Remark 2 we expect that, at least for moderate Re , this constants be $\mathcal{O}(1)$.

5.1 A test problem

In order to test our error estimator we have considered the following linear Navier-Stokes problem in the unit box $\Omega \stackrel{def}{=} (0, 1)^2$:

$$\begin{aligned} -\frac{1}{Re} \Delta \overline{u} + (\overline{u} \cdot \nabla) \overline{u} + \nabla \overline{p} &= \overline{f} && \text{in } \Omega, \\ \nabla \cdot \overline{u} &= 0 && \text{in } \Omega, \\ \overline{u} &= 0 && \text{on } \Gamma_D = \partial\Omega. \end{aligned}$$

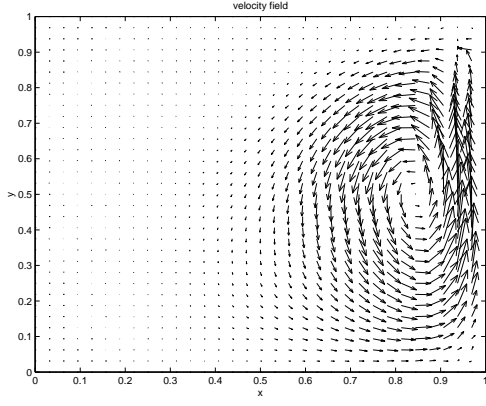


Figure 1. $R_1 = 4.2985, R_2 = 0.1$

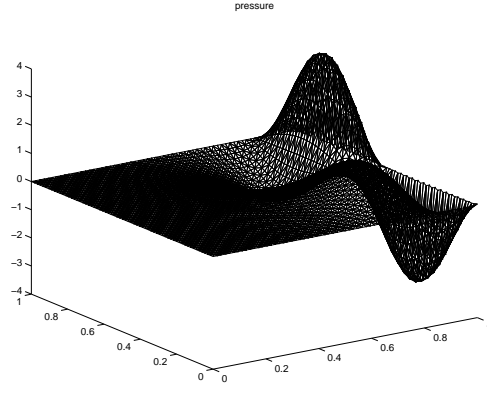


Figure 2. $R_1 = 4.2985, R_2 = 0.1$

We define the vector field $\bar{a} = [a_1, a_2]$ as follows:

$$a_1(x, y) \stackrel{def}{=} \left(1 - \cos \left(\frac{2\pi (e^{R_1 x} - 1)}{e^{R_1} - 1} \right) \right) \times \sin \left(\frac{2\pi (e^{R_2 y} - 1)}{e^{R_2} - 1} \right) \frac{R_2}{2\pi} \frac{e^{R_2 y}}{(e^{R_2} - 1)}, \quad (21)$$

$$a_2(x, y) \stackrel{def}{=} -\sin \left(\frac{2\pi (e^{R_1 x} - 1)}{e^{R_1} - 1} \right) \times \left(1 - \cos \left(\frac{2\pi (e^{R_2 y} - 1)}{e^{R_2} - 1} \right) \right) \frac{R_1}{2\pi} \frac{e^{R_1 x}}{(e^{R_1} - 1)} \quad (22)$$

where R_1, R_2 are two strictly positive real parameters. With a suitable choice of $\bar{f} = [f_1, f_2]$, the solution $[\bar{u}, p]$ of the problem is

$$u_1(x, y) = a_1(x, y), \quad (23)$$

$$u_2(x, y) = a_2(x, y), \quad (24)$$

$$p(x, y) = R_1 R_2 \sin \left(\frac{2\pi (e^{R_1 x} - 1)}{e^{R_1} - 1} \right) \sin \left(\frac{2\pi (e^{R_2 y} - 1)}{e^{R_2} - 1} \right) \times \frac{e^{R_1 x} e^{R_2 y}}{(e^{R_1} - 1)(e^{R_2} - 1)}. \quad (25)$$

Obviously, $[\bar{u}, p]$ is also the solution of the standard (non-linear) Navier-Stokes problem with the same \bar{f} . The velocity field of this solution is similar to a counterclockwise vortex in a unit-box (see Figures 1,2). Playing with the parameters R_1 and R_2 we can move the centre of this vortex that has coordinates $x_0 = \frac{1}{R_1} \log \left(\frac{e^{R_1} + 1}{2} \right)$ and $y_0 = \frac{1}{R_2} \log \left(\frac{e^{R_2} + 1}{2} \right)$. Increasing R_1 , the centre goes rapidly towards the right-hand vertical side, whereas increasing R_2 it

Re	R_1	h	$ \overline{\mathcal{T}} _1$	$\ \Psi\ _0$	$t.e.$	$e.i.$
17	0.060177	8.8388E-02	2.1475E-01	9.9644E-03	2.2462E-01	0.64262
		4.4194E-02	1.0662E-01	2.4963E-03	1.0896E-01	0.58614
		2.2097E-02	5.3273E-02	6.3073E-04	5.3833E-02	0.57271
		1.1048E-02	2.6631E-02	1.6118E-04	2.6759E-02	0.57050
34	0.700903	8.8388E-02	2.3392E-01	1.2997E-02	2.6763E-01	0.59959
		4.4194E-02	1.1054E-01	3.3034E-03	1.2367E-01	0.51469
		2.2097E-02	5.4573E-02	8.3373E-04	6.0504E-02	0.48944
		1.1048E-02	2.7202E-02	2.1025E-04	2.9989E-02	0.48359
68	1.295759	8.8388E-02	3.7340E-01	2.2786E-02	4.5952E-01	0.64799
		4.4194E-02	1.3368E-01	5.8645E-03	1.7231E-01	0.51774
		2.2097E-02	5.9664E-02	1.4835E-03	7.9991E-02	0.46034
		1.1048E-02	2.8909E-02	3.7302E-04	3.9085E-02	0.44271
136	1.883831	8.8388E-02	1.2138E+00	4.9425E-02	1.3045E+00	0.69616
		4.4194E-02	2.8285E-01	1.2812E-02	3.3278E-01	0.55793
		2.2097E-02	8.6756E-02	3.2432E-03	1.2549E-01	0.46881
		1.1048E-02	3.4549E-02	8.1441E-04	5.7136E-02	0.42379

Table 1

Convergence results on uniform triangulations

approaches the top edge.

Every numerical result that we shall present is obtained using continuous linear finite elements for both velocity and pressure. Moreover, every integral needed to set up the linear system is computed assuming $n_1 = n_2 = 3$ in (12,13); this is achieved by computing the integrals with suitable quadrature formulas on each triangle. A quadrature formula of order 5 on each element is used for computing the norms in the true error. The parameter λ appearing in the stabilizing parameter δ_T in (7) is set to 0.

5.2 Numerical results on uniform triangulations

At first, we want to study how the effectivity index $e.i.$ (19), the true error $t.e.$ (15) and each one of its components vary with the mesh-size h and the Reynolds number on a uniform grid. As a test problem we consider the case in which the centre of the vortex moves with Re on the horizontal line

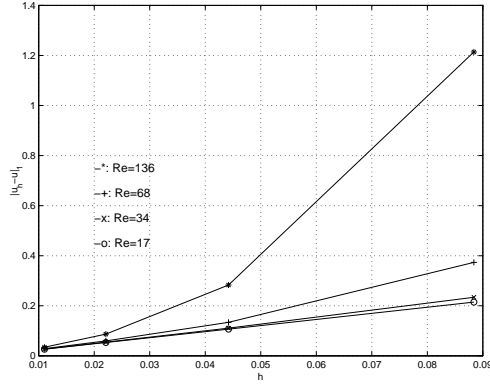


Figure 3. Uniform Grid: $\|\overline{T}\|_1$

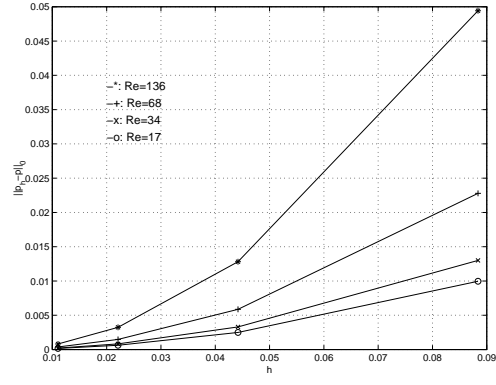


Figure 4. Uniform Grid: $\|\Psi\|_0$

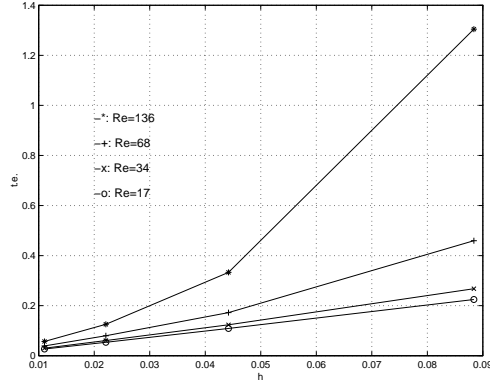


Figure 5. Uniform Grid: $t.e.$

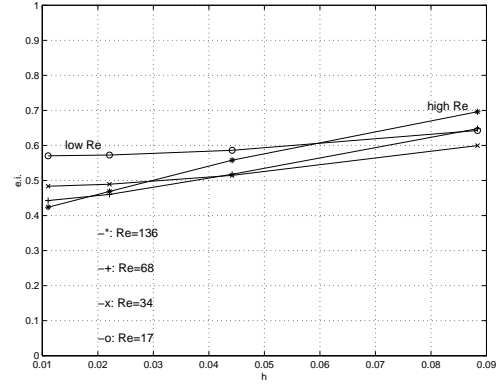


Figure 6. Uniform Grid: $e.i.$

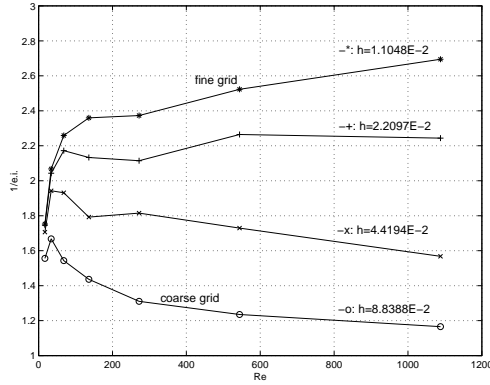


Figure 7. Uniform Grid: $1/e.i.$

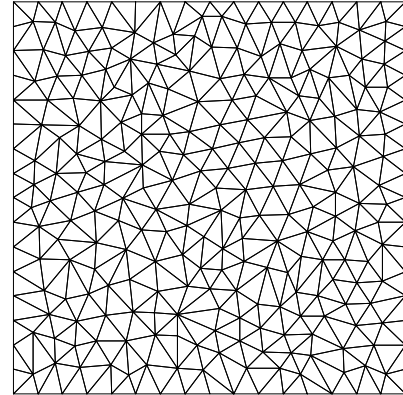


Figure 8. Example of quasi-uniform Grid: $N_{node} = 284$

$y_0 = 0.5125$ ($R_2 = 0.1$) and its distance from the right-hand vertical wall is $\frac{1}{\sqrt[4]{Re}}$. This is obtained by choosing the parameter R_1 such that $\frac{1}{R_1} \log \left(\frac{e^{R_1+1}}{2} \right) = 1 - \frac{1}{\sqrt[4]{Re}}$. From Table 1 and Figure 5 we can see that the true error $\|\overline{T}\|_1 + \|\Psi\|_0$ decays, at most, like $h^{k+\frac{1}{2}}$ as we have assumed. Moreover, for the largest considered Reynolds numbers, a super-linear behaviour of $\|\overline{T}\|_1 + \|\Psi\|_0$ is observed when in some parts of the domain the local Reynolds number is in

the order of unity or larger. Figure 6 shows that the effectivity index presents little changes with h . Figure 7 shows that the dependence on the Reynolds number of the upper bound in (17) is too pessimistic. Indeed, estimate (20) with $\underline{\mathcal{C}} = \underline{c}$ and $\overline{\mathcal{C}} = \overline{C} Re$ says that $1/e.i.$ may increase linearly with Re , but our experiments indicate that the inverse of the effectivity index tends to present a low variation for high values of this parameter. In Figure 7, we can observe a strange behaviour of the effectivity index for low Re due to the fact that the hypothesis $Re \gg 1$ introduced in (10,11) to simplify the error estimator is not completely fulfilled.

5.3 Super-convergence behaviour of the pressure

As a by-product of our analysis we have observed a somehow unexpected behaviour of the pressure error. Indeed, from Table 1 and Figures 3-4 we note that the error in the velocity $\|\overline{T}\|_1$ decays linearly with h , for h less than a certain \tilde{h} , whereas the error in the pressure $\|\Psi\|_0$ is quadratic in h for all uniform grids we used. We have considered the same problem on quasi-uniform grids like the one shown in Figure 8. These tests aimed at excluding any super-convergence effect for the pressure due to the use of some particular grid. The refining criterion used on these grids is not, as for the previous cases, to split each triangle in four nested similar triangles by adding mid-points of any edge. Instead, we generate a possibly different grid in which the area of the new triangles is about one fourth of the area of the old triangles that covered the same part of the domain. We observed that the quadratic convergence of the pressure persists on these distorted grids. For the sake of completeness, we have also considered the pure Stokes problem. With the same exact solution, we observed an $h^{\frac{3}{2}}$ -decay of the pressure error; moreover, the errors of pressure and velocity divergence are concentrated near the boundaries. With a different exact solution whose velocity is flat near all boundaries, one recovers the quadratic decay of the pressure error for the Stokes problem also. In this case $\overline{\nabla} \cdot \overline{u}_h$ as well as the pressure error near the boundaries are negligible with respect to the corresponding errors inside the domain.

6 The adaptive algorithm

Now we show how the double inequality (18) can be used to generate a finite sequence of adapted Delaunay triangulations such that the solution on the last triangulation is reliable and efficiently computable. To this end we follow the strategy of equidistribution of the error indicator presented in [3,16,17] with the appropriate changes needed for the problem under consideration. Firstly,

we start by requiring that the true relative error

$$t.r.e. \stackrel{def}{=} \frac{|\overline{\mathcal{T}}|_1 + \|\Psi\|_0}{|\overline{u}_h|_1 + \|p_h\|_0} \quad (26)$$

is bounded from above and from below in terms of a given tolerance TOL, as follows:

$$\underline{\mathcal{C}} (1 - \alpha) \text{TOL} \leq \frac{|\overline{\mathcal{T}}|_1 + \|\Psi\|_0}{|\overline{u}_h|_1 + \|p_h\|_0} \leq \overline{\mathcal{C}} (1 + \alpha) \text{TOL}, \quad (27)$$

where α is a given parameter in the range $(0, 1]$. To reach the goal of equidistributing the error, we seek to equidistribute the estimated error and to impose for each triangle the two inequalities

$$\frac{(1 - \alpha)^2 \text{TOL}^2 (|\overline{u}_h|_1 + \|p_h\|_0)^2}{N_T} \leq \eta_{R,T}^2, \quad (28)$$

$$\eta_{R,T}^2 \leq \frac{(1 + \alpha)^2 \text{TOL}^2 (|\overline{u}_h|_1 + \|p_h\|_0)^2}{N_T}. \quad (29)$$

where N_T is the number of elements in the triangulation. Combining the previous relations (27,28,29), for our adaptive algorithm, we get the following bounds for the effectivity index

$$\frac{(1 - \alpha)}{(1 + \alpha)} \frac{1}{\overline{\mathcal{C}}} \leq e.i. \leq \frac{(1 + \alpha)}{(1 - \alpha)} \frac{1}{\underline{\mathcal{C}}}, \quad (30)$$

after equidistribution of the local error estimator $\eta_{R,T}^2$ between the triangles. It is clear that the lower and upper bounds for the effectivity index are independent of the imposed tolerance and, of course, of the mesh-size, but they depend on the parameter α , i.e., on the adaptation strategy. We note that the two bounds of the effectivity index depend on the Reynolds number by means of the two “constants” $\underline{\mathcal{C}}$ and $\overline{\mathcal{C}}$. The numerical results of Subsection 5.2 suggest us that $\overline{\mathcal{C}}$ seems to be a sub-linear function of the Reynolds number.

6.1 Refining and coarsening

Now we explain how we use the target-relations (28,29) to adapt the mesh. At first, on any given mesh we calculate the solution with finite elements of order k , then for any triangle T we compute $\eta_{R,T}$. If $\eta_{R,T}^2$ is greater than the

upper bound in (29), we decide to refine this triangle, whereas if $\eta_{R,T}^2$ is less than the lower bound in (28) then we state that T could be coarsened.

The refining strategy is as follows. Let T be a triangle that has to be refined. We add the mid-point of each edge that is shared with another triangle that has to be refined. If none of the triangles having an edge in common with T has to be refined, we add only the barycentre of T . If T is a boundary element we add the mid-point of the edges shared with triangles to be refined and we always add the middle point of the boundary edges. The coarsening strategy consists of suppressing a node only if all the elements that share this node as a vertex have to be coarsened.

After this adding and suppression of points we give the list of points to the triangulator *Triangle* [20], with the optional request that the minimal angle of the new triangulations is not less than a certain value. On the new mesh we solve the problem and repeat the adaptive algorithm until the elements to be refined are less than, say, 2% of all elements and

$$\frac{\eta_{\Omega}}{|\overline{u}_h|_1 + \|p_h\|_0} \leq (1 + \alpha) \text{TOL}. \quad (31)$$

This trick is useful to avoid last adaptive iterations in which we introduce very little changes in the mesh, but we have to solve the full problem; usually this turns out to be very expensive with respect to the little increase of accuracy obtained.

6.2 Numerical results on adapted triangulations

Our test problem for adaptivity is defined like the previous one, but now we solve it on adapted triangulations. We consider different Reynolds numbers and we apply the adaptive algorithm based on the target inequalities (28,29). In Table 2 we report some meaningful quantities concerning the adaptive algorithm: the number *iter* of adapted grids built to reach the imposed tolerance, the number of nodes N_{node} , the true relative error *t.r.e.* (26) and the estimated relative error

$$e.r.e. = \frac{\eta_{\Omega}}{|\overline{u}_h|_1 + \|p_h\|_0}$$

all on the last adapted grid. Figures 9-11 exhibit the trend of these quantities during the convergence towards the target tolerance. Figures 9,10 show an evident parallel decay for the true error *t.e.* and the global error indicator η_{Ω}

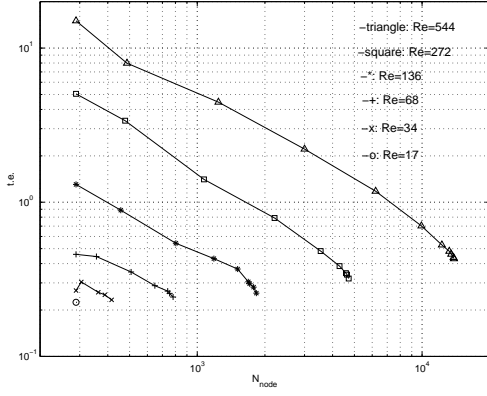


Figure 9. Adaptive case: $t.e.$

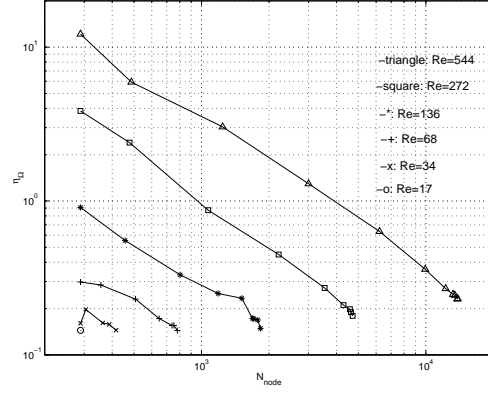


Figure 10. Adaptive case: η_{Ω}

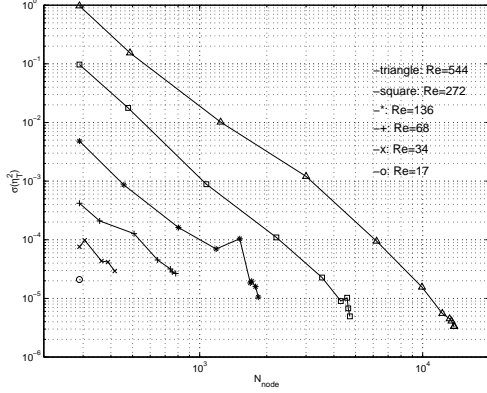


Figure 11. Adaptive case: $\sigma_{\eta_{R,T}}^2$

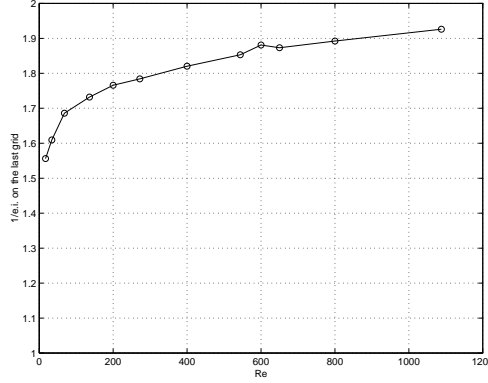


Figure 12. Adaptive case: $1/e.i.$

Re	$iter$	N_{node}	$t.r.e.$	$e.r.e.$	$e.i.$
17	1	289	1.183956E-01	7.608372E-02	0.6426
34	5	416	1.178450E-01	7.322344E-02	0.6213
68	7	781	2.237083E-01	7.452908E-03	0.5931
136	9	1832	1.044399E-01	6.030074E-02	0.5774
272	9	4719	1.094436E-01	6.134174E-02	0.5605
544	11	13865	1.213537E-01	6.548881E-02	0.5397
600	11	16238	1.234726E-01	6.564014E-02	0.5316
650	11	18793	1.230715E-01	6.570488E-02	0.5339
800	13	26584	1.243112E-01	6.569474E-02	0.5285
1088	13	45826	1.247278E-01	6.475542E-02	0.5192

Table 2

Errors analysis of the adaptive algorithm: $TOL = 0.1$, $\alpha = 0.5$

(16). In Figure 11 we report the standard deviation of $\eta_{R,T}^2$

$$\sigma_{\eta_{R,T}^2} = \sqrt{\frac{\sum_{T \in \mathcal{T}_h} (\eta_{R,T}^2 - \overline{\eta_R^2})^2}{N_T}}, \quad (32)$$

where $\overline{\eta_R^2}$ denotes the mean value of the quantity $\eta_{R,T}^2$. Its decay indicates that the adaptive algorithm really equidistributes the error around the mean value. Figure 12 and Table 2 confirm the theoretical prediction that the effectivity index is $\mathcal{O}(1)$. Furthermore, the results strengthen our opinion that the dependence on Re of the upper bound in (17) seems to be too pessimistic; indeed, $1/e.i.$ presents a very slow increase for high Reynolds numbers. When we vary Re by three orders of magnitude, we find a little variation for $1/e.i.$; the effectivity index always grows less for high Reynolds numbers than for low ones.

6.3 Nodes to get a prescribed tolerance

So far, we have discussed how our adaptive algorithm works on a test problem when we require a certain value of tolerance. It is also interesting to investigate the relationship between the prescribed tolerance and the number of grid-points needed to match this requirement (i.e., at the convergence of the adapted algorithm on the last adapted grid). Obviously, this number depends on the features of the solution. Our main target is to build an algorithm that places the grid-points in a quasi-optimal manner, i.e., that identifies the features of the solution and acts consequently. To see if our algorithm reaches this goal, we consider the previous test problem with $Re = 544$, which presents only a boundary layer at the right-hand wall. Table 3 and Figure 13 show us the relationship between the tolerance and the number of nodes; Figure

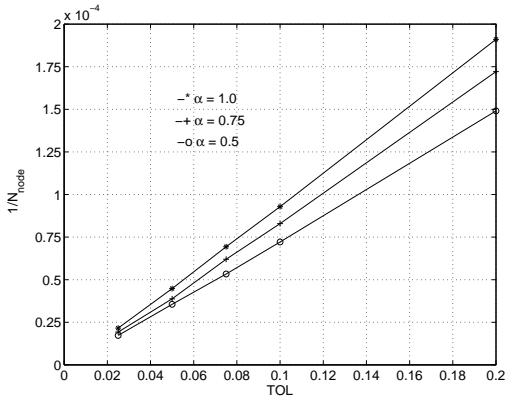


Figure 13. $\frac{1}{N_{node}}$ versus TOL

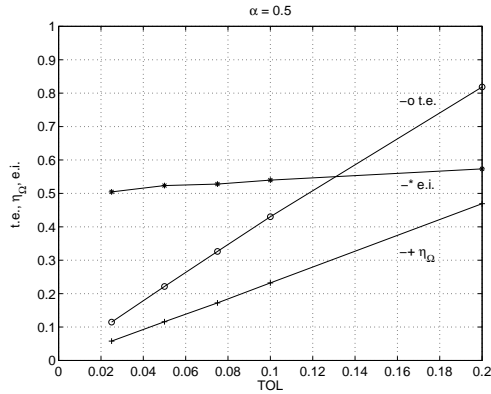


Figure 14. η_{Ω} , $t.e.$, $e.i.$ versus TOL

14 shows the behaviour of the true error, the estimated error and the effectivity index as functions of the tolerance. We observe that both the true error and the inverse of number of nodes depend approximately in a linear way on the tolerance, in the interval of TOL we have considered. This behaviour can be explained: indeed, when the prescribed tolerance is relatively large, the adaptive algorithm detects only the most relevant structures of the solution, refining only near the right-hand vertical wall; this is an “essentially 1D uniform refinement”, which yields $\frac{1}{N_{node}} \propto TOL$. As soon as the requested tolerance is small enough so that all the structures of the solution are correctly resolved on the current grid, and if there are no singularities, then the true error should reach the asymptotic behaviour of the linear dependence on the mesh-size h : thus, in term of number of nodes, for a 2D problem, we should observe $\frac{1}{N_{node}} \propto TOL^2$. However, for this problem, we could not reach this asymptotic behaviour due to computer limitations. The present experiment gives a quantitative expression to the superior performance of adaptive algorithms when the characteristic features of the solution are not completely resolved yet, as far as memory requirement is concerned. More investigations are needed to consider timing performances as well.

7 Numerical results for the non-linear incompressible Navier-Stokes model: Lid Driven Cavity

Although our previous analysis was performed for the linear Navier-Stokes model, we now apply its results to the non-linear stationary incompressible Navier-Stokes equations. We consider the classical Lid Driven Cavity problem. This problem consists of the flow in a unit square with the following velocity boundary conditions: $u_1 = 1$, $u_2 = 0$ on the top edge and $u_1 = 0$, $u_2 = 0$ on the other walls. We are interested in this problem because it is a classical test case and it allows us to consider the effect of the discontinuity in the boundary conditions on the adaptive algorithm. We compare our results for the velocity with those given in [12], that we can consider almost exact. They have been

	$\alpha = 0.5$	$\alpha = 0.75$	$\alpha = 1.0$
$TOL = 0.2$	6709	5809	5234
$TOL = 0.1$	13865	12061	10771
$TOL = 0.075$	18752	16129	14425
$TOL = 0.05$	28131	25790	22335
$TOL = 0.025$	57902	51858	46372

Table 3

Number of nodes at convergence varying TOL , $Re = 544$

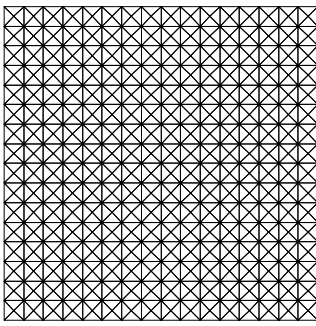


Figure 15. $N_{node} = 545$

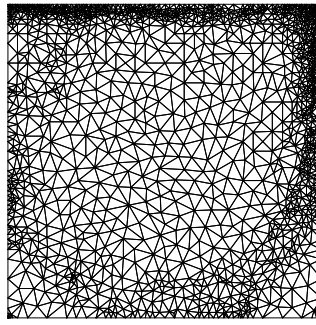


Figure 16. $N_{node} = 1883$,
 $Re = 3200$

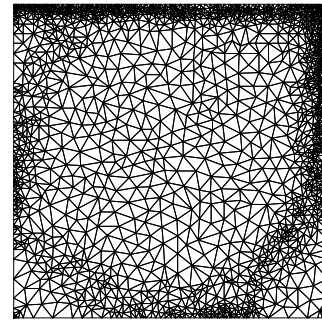


Figure 17. $N_{node} = 2156$,
 $Re = 5000$

obtained with a $\psi - \omega$ formulation of the Navier-Stokes problem, no result for the pressure is given therein.

We consider two cases at different Reynolds number: $Re = 3200$ and $Re = 5000$. To get a solution at these high Reynolds numbers we need to apply the continuation method, so we have combined continuation in Re and adaptation of the mesh. At each Re -step we solve the problem, then we perform one grid adaptation based on this solution and we use this new grid to solve the problem at the next higher Re . We set $TOL = 0.06$ and $\alpha = 0.5$. Starting with a very coarse grid with 545 nodes at $Re = 200$, we arrive at $Re = 3200$ with 1883 nodes and at $Re = 5000$ with 2156 nodes. Then, we apply our adaptive algorithm, without continuation, for the two considered Reynolds numbers, starting from the two previous partially-adapted grids. Figures 18-26 report some plots of the obtained results. Figures 18,19,20,21,24,25 display velocity profiles: u_1 along a vertical section and u_2 along an horizontal section passing through the geometric center of the cavity. The continuous line is our result and circles indicate the values reported in [12]. These reference-results are obtained with a multi-grid method on uniform meshes of $129 \times 129 = 16641$ points for $Re = 3200$ and of $257 \times 257 = 66049$ points for $Re = 5000$. We want to draw the attention on the very good agreement of our velocity results with the reference ones, also with a very small number of points, and on the good description of the two pressure singularities in the two top corners (Figures 22,23,26). Moreover, by observing the thickness of the refined region around the primary vortex in the last adapted grids (Figures 28,29) we can clearly see the decreasing of the thickness of the boundary/inner layers while increasing Re .

7.1 Adaptation at $Re = 3200$

Starting from the grid with 1883 nodes we apply the adaptive algorithm with $TOL = 0.05$ and $\alpha = 0.5$. Table 4 reports meaningful quantities of the adaptive process up to the refinement of less than 5% of the elements. We note

$iter$	N_{node}	$e.r.e.$	$\eta_{R,T,MAX}^2$	$\eta_{R,T,min}^2$	$\sigma_{\eta_{R,T}^2}$
1	1883	0.147747	3.211605E-01	3.653846E-16	6.448319E-03
2	2436	0.122983	1.319548E-01	1.770035E-11	2.888396E-03
3	3225	0.0883892	1.030873E-01	1.253682E-11	1.489866E-03
4	4039	0.0749348	9.820470E-02	3.601742E-11	1.214295E-03
5	4847	0.0733932	1.234252E-01	1.633134E-11	1.370128E-03
6	5658	0.0733819	1.281187E-01	8.087796E-12	1.315174E-03
7	6361	0.0708713	1.308443E-01	1.783953E-11	1.263084E-03
8	6998	0.0686216	1.321826E-01	1.199139E-11	1.214703E-03

Table 4

$Re = 3200$, adaptive iterations

that the adaptive algorithm produces good grids and solutions, but - due to the discontinuities of the boundary conditions - it fails to equidistribute the error in the two corners, as we can see from the very low decreasing of $\sigma_{\eta_{R,T}^2}$ (compare with Figure 11). We can easily explain this behaviour, since the discontinuities in the boundary conditions imply that the solution has strong singularities and is not in $[H_0^1(\Omega)]^2 \times L_0^2(\Omega)$, as required in deriving the error estimator.

7.2 Adaptation at $Re = 5000$

Starting from the grid with 2156 nodes we apply the adaptive algorithm with $TOL = 0.075$ and $\alpha = 0.75$ and we arrive at convergence on 98% of the triangles, with 3434 nodes. Then we apply four more adaptive steps with $TOL = 0.05$ and $\alpha = 0.75$ to arrive at convergence with these new parameters on more than 95% of the triangles. To understand how the adaptive algorithm works, let us observe Figures 24-27: although the number of points is very small, the velocity profiles are surprisingly good and the description of the secondary vortices is quite good as well. Yet the algorithm does not feel the onset of the little tertiary vortex in the bottom-right corner. Indeed the velocities here are too small ($\psi_{min} = -1.43226E - 06$) to have some relevance and the error indicator gives importance prevalently to that phenomena that cause numerically relevant errors like singularities (exactly as we wanted when we designed it).

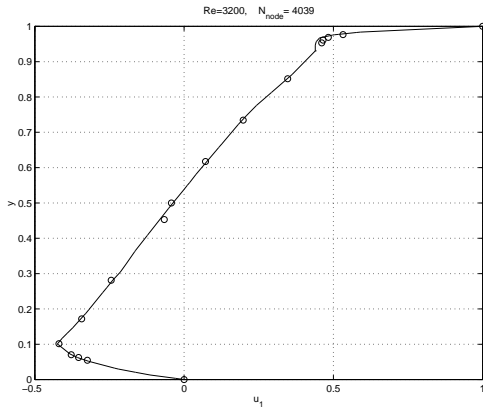


Figure 18. $x = 0.5$, component u_1

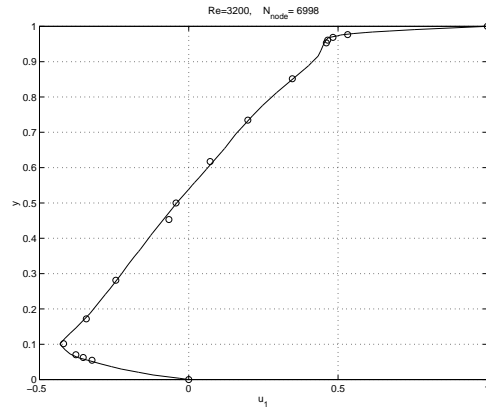


Figure 19. $x = 0.5$, component u_1

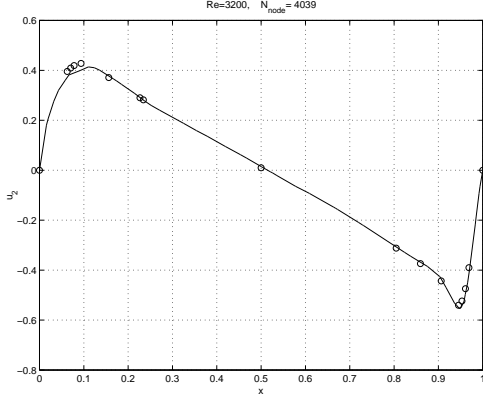


Figure 20. $y = 0.5$, component u_2

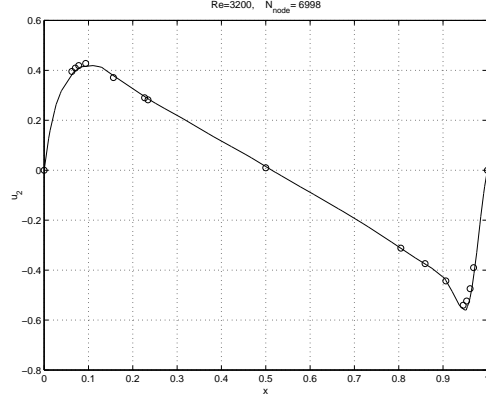


Figure 21. $y = 0.5$, component u_2

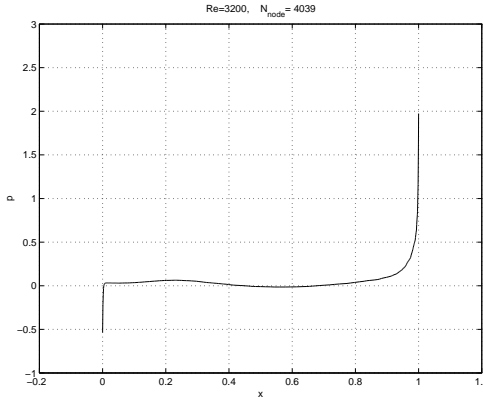


Figure 22. $y = 1.0$, pressure p

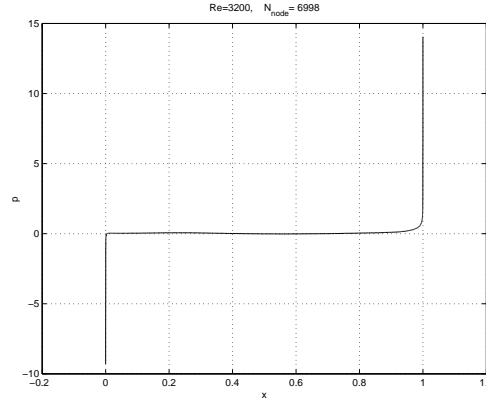


Figure 23. $y = 1.0$, pressure p

8 Conclusions

Considering all the results of our test cases, we conclude that the adaptive algorithm described in Section 6 works well. Indeed, in all our numerical experiments, it leads to refine the grid exactly where it is needed and, when possible, the equidistribution of the error between the elements is efficient, as

$iter$	N_{node}	$e.r.e.$	$\eta_{R,T,MAX}^2$	$\eta_{R,T,min}^2$	$\sigma_{\eta_{R,T}^2}$
1	2156	0.142289	3.294456E-01	6.032250E-29	6.143309E-03
2	2296	0.123102	1.295425E-01	3.001397E-12	3.115246E-03
3	2612	0.0937899	8.172397E-02	1.283356E-10	1.482653E-03
4	2926	0.0875836	1.333580E-01	3.205355E-12	2.226585E-03
5	3214	0.0893035	1.579566E-01	5.796903E-11	2.482492E-03
6	3434	0.0849747	1.253354E-01	3.222002E-12	2.191617E-03

Table 5

$Re = 5000$, adaptive iterations: $TOL = 0.075$, $\alpha = 0.75$

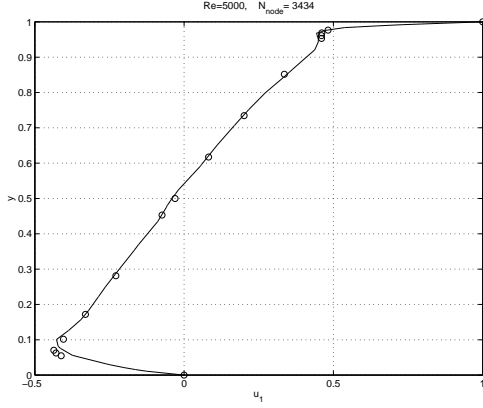


Figure 24. $x = 0.5$, component u_1

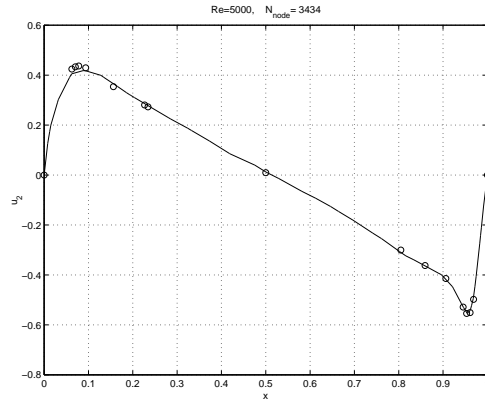


Figure 25. $y = 0.5$, component u_2

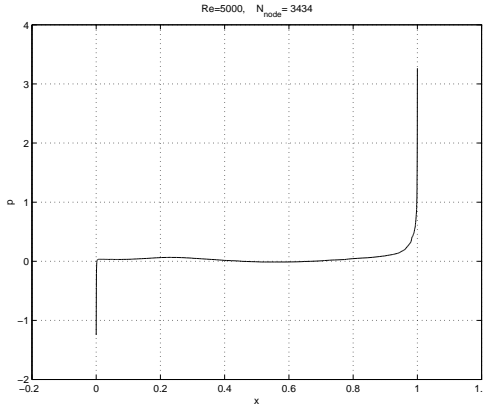


Figure 26. $y = 1.0$, pressure p

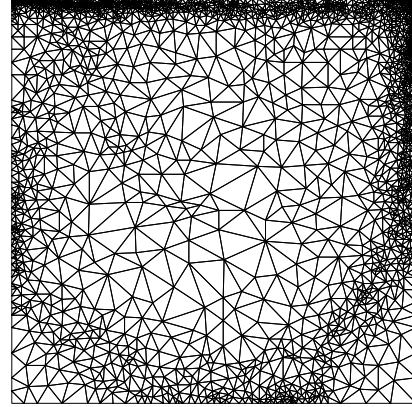


Figure 27. $Re = 5000$, $N_{node} = 3434$

we deduce from the decreasing behaviour of the standard deviation $\sigma_{\eta_{R,T}^2}$ (Figure 11). We also notice that the computation of such low-cost error estimator, combined with the numerical estimates of the constants involved (which, from our experiments, turn out to be in the order of the unity), is useful to get a measure of the quality of the solution, independently of the adaptive strategy used.

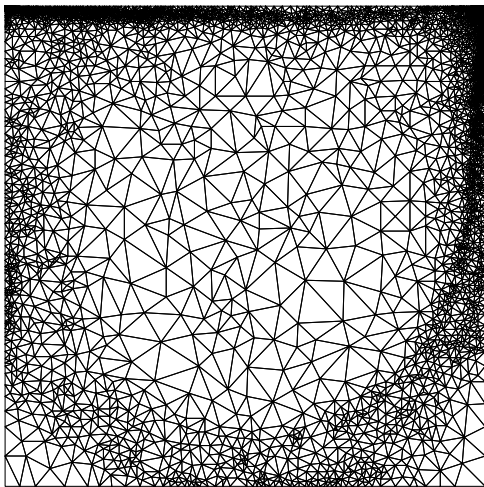


Figure 28. $Re = 3200$, $N_{node} = 6998$

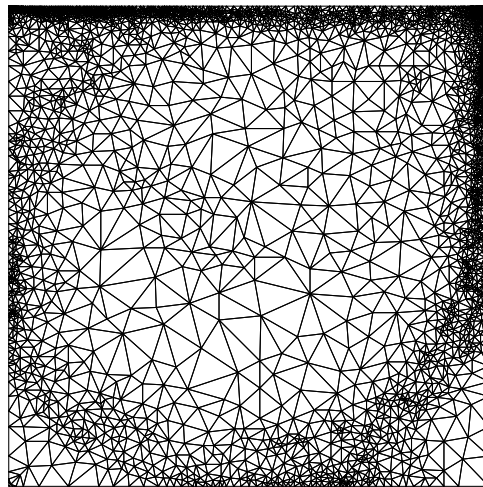


Figure 29. $Re = 5000$, $N_{node} = 6247$

Finally we observe that the maximal performance of adaptivity versus uniform refinement and versus “by hand” mesh adaptation is achieved in problems that present characteristic structures in a limited part of the domain. When the characteristic features of the solution are distributed in a wide part of the domain, the superiority of adaptive algorithms is reduced [4], but the advantage of building automatically a quasi-optimal grid in terms of number of degrees of freedom persists. Moreover, on this grid we are sure that the relative error in the computed solution could be controlled by a target tolerance, that we can choose suitably in relation to the necessities of each problem.

Acknowledgement

The author would like to thank the Department of Mathematics of the Politecnico di Torino for allowing him the use of all its facilities. Special thanks are due to Giuseppe Ghibò, system administrator at the Department, for his essential support in carrying out the numerical computations. The author is greatly obliged to his advisor Prof. Claudio Canuto for introducing him to these subjects, for his patient and precious help and for his careful reading of the manuscript.

References

- [1] M. Ainsworth, J.T. Oden *A posteriori error estimation in finite element analysis*, Comput. Methods Appl. Mech. Engrg. 142 (1997), 1-88.
- [2] I. Babuška, R. Durán, R. Rodríguez, *Analysis of the efficiency of an a posteriori*

- error estimator for linear triangular elements*, SIAM J. Numer. Anal. 29 (1992), no. 4, 947-964.
- [3] I. Babuška, W.C. Rheinboldt, *Error estimates for adaptive finite element method*, SIAM J. Numer. Anal. 15 (1978), no. 4, 736-754.
 - [4] S. Berrone, *Adaptive discretization of the Navier Stokes equations by stabilized Finite Element Method*, Rapporto interno N. 7, 1999, Dipartimento di Matematica, Politecnico di Torino, available on the author's home page.
 - [5] F. Brezzi, M.O. Bristeau, L.P. Franca, M.M. Mallet, G. Rogé, *A relationship between stabilized finite element methods and the Galerkin method with bubble functions*, Comput. Methods Appl. Mech. Engrg. 96 (1992), 117-129.
 - [6] F. Brezzi, M. Fortin, *Mixed and Hibrid Finite Element Methods*, Springer-Verlag, New York-Berlin, 1991.
 - [7] C. Canuto, A. Russo, V. Van Kemenade, *Stabilized spectral methods for the Navier-Stokes equations: residual-free bubbles and preconditioning*, Comput. Methods Appl. Mech. Engrg. 166 (1998), 65-83.
 - [8] P.G. Ciarlet, *The Finite Element Method for Elliptic Problems*, North-Holland Publishing Company, Amsterdam, 1978.
 - [9] K. Eriksson, D. Estep, P. Hansbo, C. Johnson, *Introduction to adaptive methods for differential equations*, Acta Numerica (1995), 105-158. Cambridge University Press, Cambridge, 1995.
 - [10] L.P. Franca, S.L. Frey, *Stabilized finite element methods: II. The incompressible Navier-Stokes equations*, Comput. Methods Appl. Mech. Engrg. 99 (1992), 209-233.
 - [11] L.P. Franca, S.L. Frey, T.J.R. Hughes, *Stabilized finite element methods: I. Application to the advective-diffusion model*, Comput. Methods Appl. Mech. Engrg. 95 (1992), 253-276.
 - [12] U. Ghia, K.N. Ghia, C.T. Shin, *High-Re solutions for incompressible flow using the Navier-Stokes equations and a multigrid method*, J. Comput. Phys. 48 (1982), 387-411.
 - [13] V. Girault, P.A. Raviart, *Finite Element Methods for Navier-Stokes Equations, Theory and Algorithms*, Springer-Verlag, Berlin Heidelberg, 1986.
 - [14] I. Harari, T.J.R. Hughes, *What are C and h ?: Inequalities for the analysis and design of finite element methods*, Comput. Methods Appl. Mech. Engrg. 97 (1992), 157-192.
 - [15] T.J.R. Hughes, L.P. Franca, M. Balestra *A new finite element formulation for computational fluid dynamics: V. Circumventing the Babuška-Brezzi condition: A stable Petrov-Galerkin formulation of the Stokes problem accommodating equal-order interpolations*, Comput. Methods Appl. Mech. Engrg. 59 (1986), 85-99.

- [16] C. Johnson, *Adaptive finite element methods for diffusion and convection problems*, Comput. Methods Appl. Mech. Engrg. 82 (1990), 301-322.
- [17] J. Medina, M. Picasso, J. Rappaz, *Error estimates and adaptive finite elements for nonlinear diffusion-convection problems*, Math. Models Methods Appl. Sci. 6 (1996), 689-712.
- [18] H.G. Roos, M. Stynes, L. Tobiska, *Numerical Methods for Singularly Perturbed Differential Equations, Convection-Diffusion and Flow Problems*, Springer-Verlag, Berlin Heidelberg, 1996.
- [19] A. Russo, *A posteriori error estimators via bubble functions*, Math. Models. and Math. in Appl. Sci. 6 (1996), 33-41.
- [20] J. R. Shewchuk, *Part of Archimedes project*, School of Computer Science, Carnegie Mellon University, Pittsburgh, 1996.
- [21] J.R. Stewart, T.J.R. Hughes, *A tutorial in elementary finite element error analysis: A systematic presentation of a priori and a posteriori error estimates*, Comput. Methods Appl. Mech. Engrg. 158 (1998), 1-22.
- [22] L. Tobiska, R. Verfürth, *Analysis of a Streamline Diffusion Finite Element Method for the Stokes and Navier-Stokes Equations*, SIAM J. Numer. Anal. 33 (1996), no. 1, 107-127.
- [23] R. Verfürth, *A posteriori error estimators for Stokes equations*, Numer. Math. 55 (1989), 309-325.
- [24] R. Verfürth, *A posteriori error estimation and adaptive mesh-refinement techniques*, J. Comput. Appl. Math. 50 (1994), 67-83.
- [25] R. Verfürth, *A posteriori error estimates for nonlinear problems. Finite element discretization of elliptic equations*, Math. Comput. 62 (1994), 445-475.
- [26] R. Verfürth, *A Review of A Posteriori Error Estimation and Adaptive Mesh-Refinement Techniques*, John Wiley & Sons, Chichester-New York, 1996.
- [27] R. Verfürth, *Robust a posteriori error estimators for singularly perturbed reaction-diffusion equation*, Numer. Math. 78 (1998), 479-493.
- [28] R. Verfürth, *A posteriori error estimators for convection-diffusion equations*, Numer. Math. 80 (1998), 641-663.